

Imaging hydrodynamic electrons flowing without Landauer–Sharvin resistance

<https://doi.org/10.1038/s41586-022-05002-7>

Received: 7 November 2021

Accepted: 21 June 2022

Published online: 7 September 2022

 Check for updates

C. Kumar^{1,7}, J. Birkbeck^{1,7}, J. A. Sulpizio^{1,7}, D. Perello^{2,3}, T. Taniguchi⁴, K. Watanabe⁴, O. Reuven¹, T. Scaffidi^{5,6}, Ady Stern¹, A. K. Geim^{2,3} & S. Ilani¹✉

Electrical resistance usually originates from lattice imperfections. However, even a perfect lattice has a fundamental resistance limit, given by the Landauer¹ conductance caused by a finite number of propagating electron modes. This resistance, shown by Sharvin² to appear at the contacts of electronic devices, sets the ultimate conduction limit of non-interacting electrons. Recent years have seen growing evidence of hydrodynamic electronic phenomena^{3–18}, prompting recent theories^{19,20} to ask whether an electronic fluid can radically break the fundamental Landauer–Sharvin limit. Here, we use single-electron-transistor imaging of electronic flow in high-mobility graphene Corbino disk devices to answer this question. First, by imaging ballistic flows at liquid-helium temperatures, we observe a Landauer–Sharvin resistance that does not appear at the contacts but is instead distributed throughout the bulk. This underpins the phase-space origin of this resistance—as emerging from spatial gradients in the number of conduction modes. At elevated temperatures, by identifying and accounting for electron–phonon scattering, we show the details of the purely hydrodynamic flow. Strikingly, we find that electron hydrodynamics eliminates the bulk Landauer–Sharvin resistance. Finally, by imaging spiralling magneto-hydrodynamic Corbino flows, we show the key emergent length scale predicted by hydrodynamic theories—the Gurzhi length. These observations demonstrate that electronic fluids can dramatically transcend the fundamental limitations of ballistic electrons, with important implications for fundamental science and future technologies.

When an electron flowing in an electrical device collides with an impurity, a phonon or a rough edge, it loses momentum to the lattice, generating resistance. Surprisingly, even when these scattering sources are eliminated, electronic devices still have a Landauer–Sharvin resistance^{1,2}, resulting from the finite conduction capacity of a channel, given by the number of its conduction modes multiplied by e^2/h (where e is the electronic charge and h is Planck's constant). This resistance appears at the interface between the device and its contacts, where the number of conduction modes changes sharply. The Landauer–Sharvin resistance thus sets the ultimate resistance limit for ballistic electrons and gives a performance bound for real-life devices, at which electrons are forced to transition frequently between metals and semiconductors.

Theoretical^{21–32} and experimental^{3–18} evidence suggests that when the interaction between electrons is sufficiently strong, the electronic system behaves as a hydrodynamic fluid. Transport measurements of hydrodynamic electrons flowing through constrictions⁷ showed up to 15% better conductivity than their ballistic counterparts, explained theoretically²⁸ by hydrodynamic lubrication of the constriction's walls. This raises a question of fundamental and practical importance^{19,20}:

if the Landauer–Sharvin resistance limits ballistic electrons, what is the ultimate conduction limit for hydrodynamic electrons?

In this Article, we show experimentally that hydrodynamic electrons can dramatically outperform the limitations of ballistic electrons. By imaging electronic flows in a Corbino disk geometry, we observe that for ballistic electrons roughly half of their Landauer–Sharvin resistance is distributed throughout the bulk of the device rather than at the interfaces with the contacts. At elevated temperatures, we find that electron hydrodynamics efficiently eliminates this ‘bulk Landauer–Sharvin’ resistance, consistent with the ideal hydrodynamic elimination of the spread Landauer–Sharvin resistance, which is predicted theoretically²⁰. At small magnetic fields, electron spiralling generates a viscous boundary layer near the contacts, providing a real-space observation of the Gurzhi length. Our findings demonstrate that hydrodynamics can dramatically modify the well-established rules obeyed by ballistic electrons.

Consider ballistic transport through two geometries: a straight channel (Fig. 1a) and a Corbino disk (Fig. 1b). In both cases, the total device resistance is given by the Landauer–Sharvin resistance: for a channel it is $R_{\text{sh}} = \frac{\pi h}{4e^2 k_F W}$ (W is channel width and k_F is the Fermi momentum) and for a Corbino disk it is $R_{\text{sh}}^{\text{in}} = \frac{\pi h}{4e^2 k_F (2\pi r_{\text{in}})}$ (where $2\pi r_{\text{in}}$ is the inner

¹Department of Condensed Matter Physics, Weizmann Institute of Science, Rehovot, Israel. ²School of Physics & Astronomy, University of Manchester, Manchester, UK. ³National Graphene Institute, University of Manchester, Manchester, UK. ⁴National Institute for Materials Science, Tsukuba, Japan. ⁵Department of Physics, University of Toronto, Toronto, ON, Canada. ⁶Department of Physics and Astronomy, University of California, Irvine, CA, USA. ⁷These authors contributed equally: C. Kumar, J. Birkbeck, J. A. Sulpizio. ✉e-mail: shahal.ilani@weizmann.ac.il

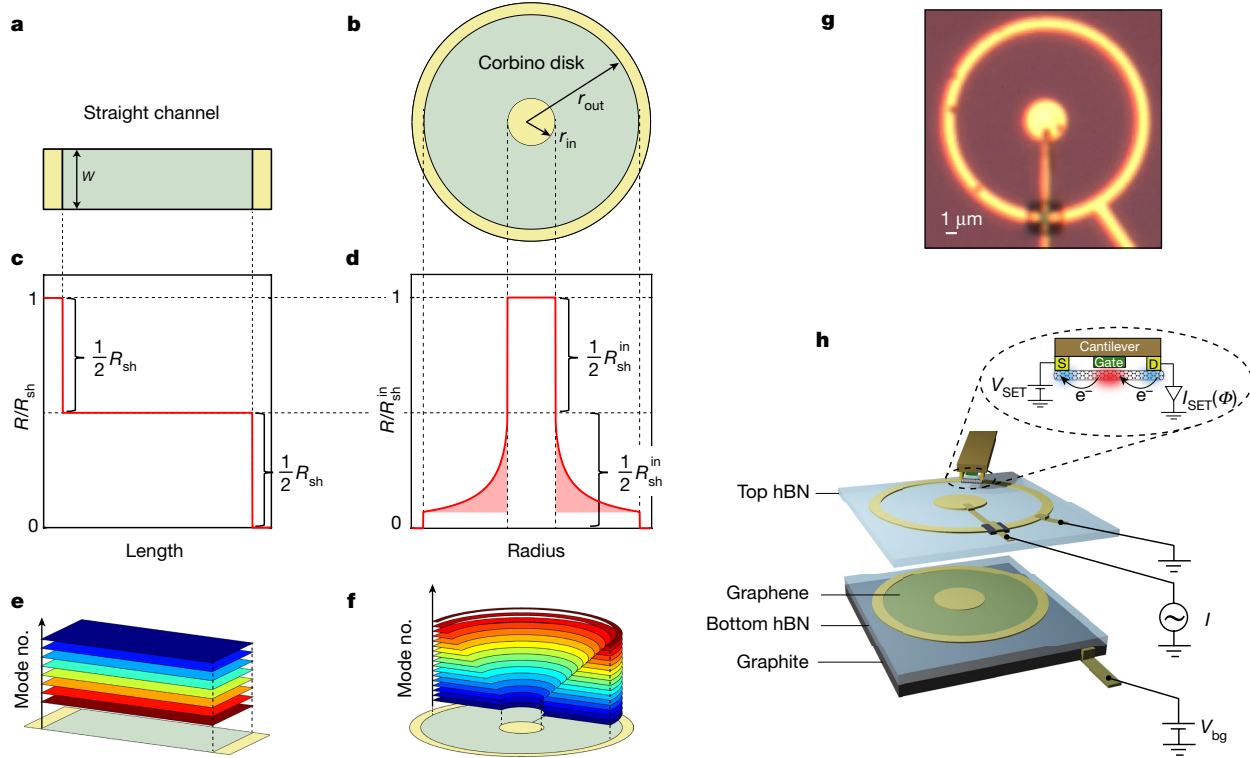


Fig. 1 | Landauer–Sharvin bulk geometrical resistance and the experimental setup for its measurement. a, b, Comparing two channel geometries, a straight channel (**a**, with the channel in green and contacts in yellow) and a Corbino disk channel (**b**, where the inner and outer radii are r_{in} and r_{out} , respectively). In the ballistic limit (no scattering, perfect edges) the total (two-probe) resistance of both geometries is inversely proportional to the number of conduction modes traversing the device, multiplied by e^2/h . For a straight graphene channel, this gives $R_{sh} = \frac{\pi h}{4e^2 k_F W}$ (W is the channel width and k_F is the Fermi momentum). For a Corbino disk, W is replaced by the inner contact circumference, $R_{sh}^{in} = \frac{\pi h}{4e^2 k_F (2\pi r_{in})}$. **c,** In the straight channel, half of the Landauer–Sharvin resistance drops sharply at each contact interface and there is no resistive drop in the bulk. **d,** In the Corbino disk, half the Landauer–Sharvin

resistance drops on the inner contact, but the other half is distributed throughout the bulk. The Landauer–Sharvin resistance is fundamentally connected to the spatial gradient in the number of conduction modes. **e,** In a straight channel, this number is constant throughout the bulk but changes sharply at the contact interfaces. **f,** In a Corbino disk, there is a linear increase of the number of modes with radius, leading to the bulk Landauer–Sharvin resistance. **g,** Optical image of one of the studied devices ($r_{in} = 2 \mu\text{m}$, $r_{out} = 9 \mu\text{m}$). **h.** The device is composed of top hBN, graphene, bottom hBN and a graphite back gate, with inner (circular) and outer (ring) contacts. The carrier density is tuned by back-gate voltage, V_{bg} . Scanning nanotube-based SET (inset) images the potential (Φ) in the device while current I_{SET} flows between the contacts (Source (S) and Drain (D), with bias V_{SET}).

circumference). In a straight channel, half of this resistance drops at each contact interface (Fig. 1c). Interestingly, in a Corbino disk, whereas half of the Landauer–Sharvin resistance drops at the inner contact interface, the other half is predicted to distribute across the bulk of the device^{19,20} (Fig. 1d).

This distributed Landauer–Sharvin resistance highlights its geometrical/phase-space origin—this resistance appears when there is a spatial gradient in the number of conduction modes within the device. In a straight channel, the number of modes changes sharply at the contact interfaces but is fixed throughout the bulk (Fig. 1e). By contrast, in a Corbino disk, this number decreases with decreasing radius (Fig. 1f and Supplementary Section 16), resulting in a distributed bulk Landauer–Sharvin resistance. The latter reflects the gradually shrinking phase space experienced by an electron travelling from the outer to the inner contact.

Interestingly, recent theory¹⁹ suggested that in a Corbino geometry hydrodynamic electrons will eliminate the bulk half of the Landauer–Sharvin resistance. A new generalized analysis²⁰ showed that the Landauer–Sharvin resistance is directly connected to the spatial gradient in the number of conducting modes and that it originates from the reflection enforced on electrons in terminated modes. Electron–electron scattering enables these electrons to smoothly transfer from a mode that is about to be terminated to a propagating mode, thus reducing the resistance. This analysis predicted that, for hydrodynamic electrons, resistance occurs only where the number of modes has a

non-zero second spatial derivative²⁰. As in a Corbino disk the number of modes increases linearly with distance, this geometry is the ideal testbed to examine the elimination of the Landauer–Sharvin resistance by hydrodynamic flows.

Our devices consist of high-mobility hBN (hexagonal boron nitride)-encapsulated monolayer graphene patterned into a Corbino disk geometry, with a graphite back gate that tunes the carrier density, n . The graphene spans a disk between radii r_{in} and r_{out} , where it connects to Cr/Au contacts. The inner contact is connected via a line deposited on top of a crossed-linked resist patch, above the top hBN layer, to not perturb the angular symmetry of the graphene disk (Supplementary Section 1). We present data from a device with $r_{in} = 2 \mu\text{m}$ and $r_{out} = 9 \mu\text{m}$ in Fig. 1g. Similar results were obtained on a second Corbino device with different dimensions (Supplementary Section 8).

A major advantage of a Corbino geometry over Hall-bar devices is the absence of etched edges and lithographically defined voltage probes. This eliminates spurious scattering at these features, enabling us to measure the unperturbed electron flow. This advantage comes at a price: transport experiments can measure only the two-probe device resistance but cannot decipher its spatial distribution. To overcome this, we use a nanotube-based scanning single-electron transistor³³ (SET) to spatially map the potential drop associated with the electronic current³⁴. We drive an a.c. current, I , between the inner and outer Corbino contacts and use the SET to image the local electrostatic potential modulations at this a.c. frequency (Fig. 1h, frequency approximately

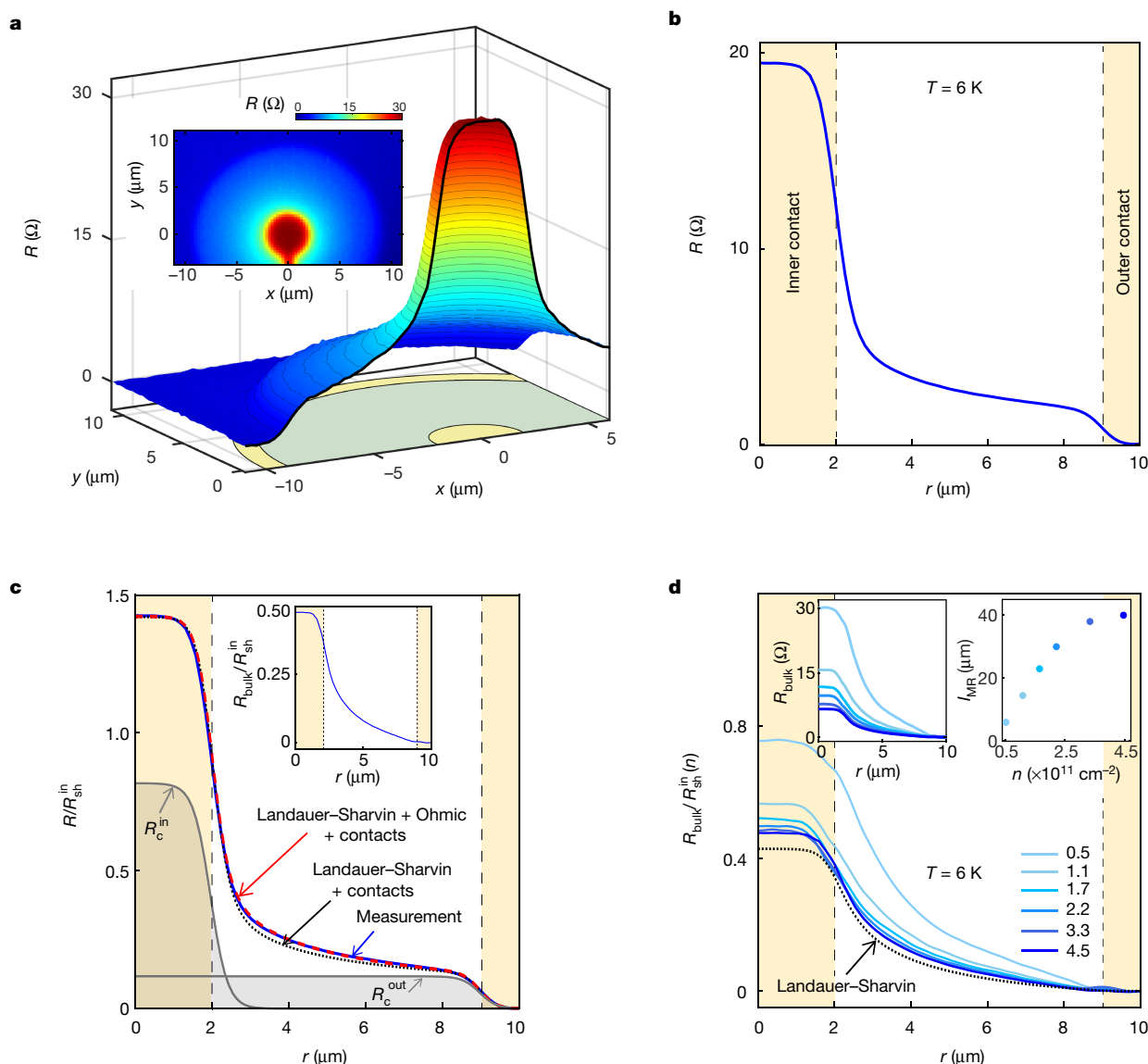


Fig. 2 | Imaging the Landauer–Sharvin bulk resistance in a Corbino disk.

a, Spatially resolved image of the resistance $R(x, y) = \phi(x, y)/I$, overlaid on the Corbino device schematics ($T = 140$ K, $n = 4.5 \times 10^{11} \text{ cm}^{-2}$). Inset: same measurement in a colour map. The measurement exhibits excellent angular symmetry, enabling us to average along the angular direction and obtain $R(r)$. **b**, $R(r)$ measured at $T = 6$ K, $n = 4.5 \times 10^{11} \text{ cm}^{-2}$ (contacts, yellow). **c**, Disentangling the various components of the resistance: blue curve, same as in **b**, but normalized by $R_{\text{sh}}^{\text{in}}$; $R_{\text{c}}^{\text{in}}(r)$ and $R_{\text{c}}^{\text{out}}(r)$ (grey curves) are step functions positioned at the contact interfaces with the graphene, $r = r_{\text{in}}$ and $r = r_{\text{out}}$, smeared by the PSF of the imaging experiment, measured separately (Supplementary Section 4). The dotted black line is a fit of the measurement to $R_{\text{LS}}(r) + R_{\text{c}}^{\text{in}}(r) + R_{\text{c}}^{\text{out}}(r)$.

1 kHz, which is much slower than transport scales). This distinguishes the potential drop associated with the current from the static disorder potential, measured independently in d.c. (direct current) in the absence of current. Our spatial resolution is limited by the scanning height above the device (around 800 nm). In the figures below (Figs. 2a–4), we plot the imaged potential normalized by the total current, $R(x, y) = \phi(x, y)/I$, where $\phi(x, y)$ and I are the measured potential and current, respectively, and define $\phi(r_{\text{out}}) = 0$, capturing the accumulated resistance in the bulk (Supplementary Section 17).

An imaged map of $R(x, y)$ (Fig. 2a) shows that it rises monotonically from the outer to the inner contact. $R(x, y)$ exhibits excellent angular symmetry at all studied temperatures, densities and magnetic fields

where $R_{\text{LS}}(r) = \frac{R_{\text{sh}}^{\text{in}}}{\pi} \arcsin\left(\frac{r_{\text{in}}}{r}\right)$ is the theoretically predicted Landauer–Sharvin bulk resistance. The dashed red line is a fit to a similar function which includes, in addition, an ohmic term, $R_{\text{ohm}}(r)/R_{\text{sh}}^{\text{in}} = \frac{2r_{\text{in}}}{\pi l_{\text{MR}}} \log\left(\frac{r_{\text{in}}}{r}\right)$, with a momentum-relaxing mean-free path of $l_{\text{MR}} = 40 \text{ } \mu\text{m}$. Inset: the bulk component of the resistance, obtained by subtracting the fitted contact resistance curves from the measurement, $R_{\text{bulk}}(r) = R(r) - (R_{\text{c}}^{\text{in}}(r) + R_{\text{c}}^{\text{out}}(r))$. **d**, Left inset, $R_{\text{bulk}}(r)$ at various carrier densities (see key). Main panel: same curves, but each normalized by the Sharvin resistance at the corresponding density, $R_{\text{sh}}^{\text{in}}(n)$. Dotted line, $R_{\text{LS}}(r)$. Right inset: l_{MR} versus n obtained from fitting the graphs in the main panel to $R_{\text{LS}}(r) + R_{\text{ohm}}(r)$.

(Fig. 2a, inset and Supplementary Section 3), enabling us to average over the angular direction to obtain the radial resistance profile, $R(r)$.

Ballistic flow: observation of bulk Landauer–Sharvin resistance

At low temperatures, transport is expected to be ballistic. Figure 2b shows $R(r)$ measured at $T = 6$ K and $n = 4.5 \times 10^{11} \text{ cm}^{-2}$. Visibly, $R(r)$ starts flat at the outer contact, rises rapidly around $r = r_{\text{out}}$, climbs gradually throughout the bulk of the Corbino disk, rises rapidly again around $r = r_{\text{in}}$ and finally flattens out at the inner contact. From this graph, we obtain a total (two-probe) device resistance of $R_{\text{tot}} = 19.5 \text{ } \Omega$. Normalized

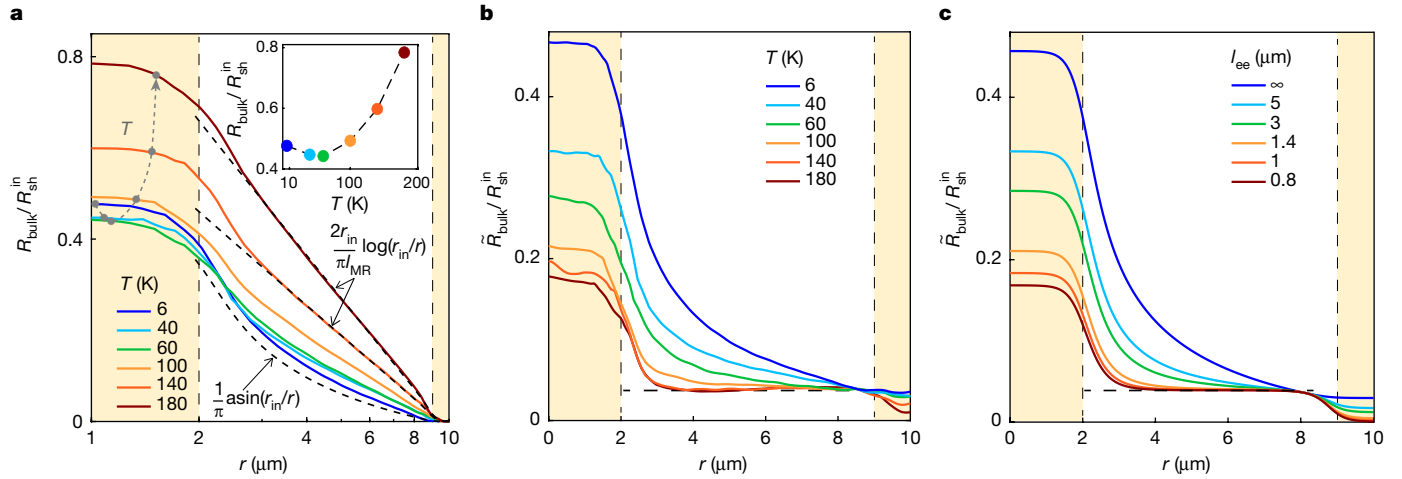


Fig. 3 | Observation of the perfect elimination of Landauer–Sharvin bulk resistance by hydrodynamic electron flow. a, $R_{\text{bulk}}(r)/R_{\text{sh}}^{\text{in}}$ measured at various temperatures, T (see key) with a logarithmic r axis. Similar to Fig. 2, $R_{\text{bulk}}(r)$ is obtained from the measured $R(r)$ by removing the contact resistance contributions. The same contact resistances (those at $T = 6$ K) were removed from all graphs. The total bulk resistance first decreases with increasing T and then only mildly increases (grey dashed line). The r dependence of the resistance evolves from Landauer–Sharvin dependence (bottom dashed line), at $T = 6$ K, to a logarithmic dependence (top dashed line), at $T = 180$ K with a small deviation only very close to the inner contact (at most $1 \mu\text{m}$). Inset: total bulk resistance normalized by $R_{\text{sh}}^{\text{in}}$ as a function of T . **b**, The clean-limit hydrodynamic flow profiles, $\tilde{R}_{\text{bulk}}(r)$, at various T , obtained from the data in **a**

by the Landauer–Sharvin resistance (Fig. 2c, blue), the measured total resistance $R_{\text{tot}} = 1.42R_{\text{sh}}^{\text{in}}$ is a bit larger than this ideal limit, owing to $T_{\text{contact}} \approx 0.75$ contact transparency³⁶ (Supplementary Section 5).

Our imaging now enables us to decompose the measured resistance into its different components. The contact interface resistance shows up as step functions at $r = r_{\text{in}}, r_{\text{out}}$, smeared by the point-spread function (PSF) of our imaging. The PSF is accurately determined by a complementary measurement (Supplementary Section 4), and thus the only free parameter in the contact resistance step functions ($R_{\text{c}}^{\text{in}}(r)$, $R_{\text{c}}^{\text{out}}(r)$ in Fig. 2c) is their height.

Remarkably, if we fit the measured $R(r)$ (blue, Fig. 2c) to $R_{\text{LS}}(r) + R_{\text{c}}^{\text{in}}(r) + R_{\text{c}}^{\text{out}}(r)$ (dotted black, Fig. 2c), where $R_{\text{LS}}(r) = \frac{R_{\text{sh}}^{\text{in}}}{\pi} \arcsin\left(\frac{r_{\text{in}}}{r}\right)$ is the theoretically predicted dependence of the Landauer–Sharvin bulk resistance^{19,20}, we find extremely close agreement. The remaining small difference (around 10%) is accounted (red dashed) by adding an ohmic term with a long mean-free path ($l_{\text{MR}} = 40 \mu\text{m}$, see below). Note that the smeared contact functions, $R_{\text{c}}^{\text{in}}(r)$ and $R_{\text{c}}^{\text{out}}(r)$, penetrate little into the bulk and therefore do not affect the quality of the fit in the bulk. The observed close agreement is especially impressive given that the expression for the Landauer–Sharvin bulk resistance has no free parameters. This measurement, therefore, provides real-space evidence of a distributed bulk Landauer–Sharvin resistance, originating from a spatial gradient of the number of conduction modes.

Figure 2d shows the measured dependence of the resistance profile on carrier density. Here, and in the rest of the Article, we plot the bulk part of the resistance obtained by subtracting the contact resistance steps from the measured profile, $R_{\text{bulk}}(r) = R(r) - (R_{\text{c}}^{\text{in}}(r) + R_{\text{c}}^{\text{out}}(r))$. This quantity gives the most accurate description of the bulk resistance profile because it eliminates the smeared tails of the contacts step functions. The left inset of Fig. 2d shows $R_{\text{bulk}}(r)$ measured at various carrier densities. The total bulk resistance varies by about a factor of four over the measured density range. However, when the resistance is normalized by $R_{\text{sh}}^{\text{in}}$ at the corresponding density, which scales as the number of conduc-

tion channels $k_{\text{F}} \propto \sqrt{n}$, all curves collapse to a similar dependence (Fig. 2d, main panel) close to the Landauer–Sharvin expression (dotted). This demonstrates that at $T = 6$ K the Landauer–Sharvin bulk resistance is the dominant contribution over a wide range of n . The difference from $R_{\text{LS}}(r)$ is well fitted by adding an ohmic term, $R_{\text{ohm}}(r) = R_{\text{sh}}^{\text{in}} \frac{2r_{\text{in}}}{\pi l_{\text{MR}}} \log\left(\frac{r_{\text{in}}}{r}\right)$, where l_{MR} is the momentum-relaxing mean-free path due to impurity scattering. The obtained n dependence of l_{MR} (Fig. 2d, right inset) is in good agreement with previous measurements^{12,14,35}.

Hydrodynamic flow: elimination of the Landauer–Sharvin resistance

We now turn to elevated temperatures, at which both electron–phonon and electron–electron scattering are enhanced. The former is momentum relaxing and is thus expected to increase the device’s ohmic resistance. Naively, one may expect the total resistance to increase with the added ohmic resistance. The measured temperature dependence (Fig. 3a) shows surprisingly different behaviour. The figure plots the measured $R_{\text{bulk}}(r)$ at temperatures $T = 6$ – 180 K, where in all curves we subtracted the same contact resistance steps (obtained at $T = 6$ K, Fig. 2c). Instead of increasing with T , the total resistance first decreases to a minimum at $T \approx 60$ K and then mildly increases towards $T = 180$ K (Fig. 3a, inset). The measured r dependence of $R_{\text{bulk}}(r)$, plotted on a logarithmic r axis in Fig. 3a, provides a hint for the underlying physics: whereas at low T it is curved, as expected from an $\arcsin(r_{\text{in}}/r)$ dependence (bottom dashed line), at $T = 140$ K and 180 K it follows a straight line almost throughout the entire bulk (middle and top dashed lines), indicating an ohmic $\log(r_{\text{in}}/r)$ dependence. This change suggests that, as the ohmic electron–phonon contribution builds up, the Landauer–Sharvin bulk resistance disappears.

The unavoidable presence of electron–phonon scattering at elevated temperatures requires us to separate its contribution to the resistance from that of the hydrodynamic electron–electron scattering. Here the angular symmetry of the Corbino geometry proves advantageous, by

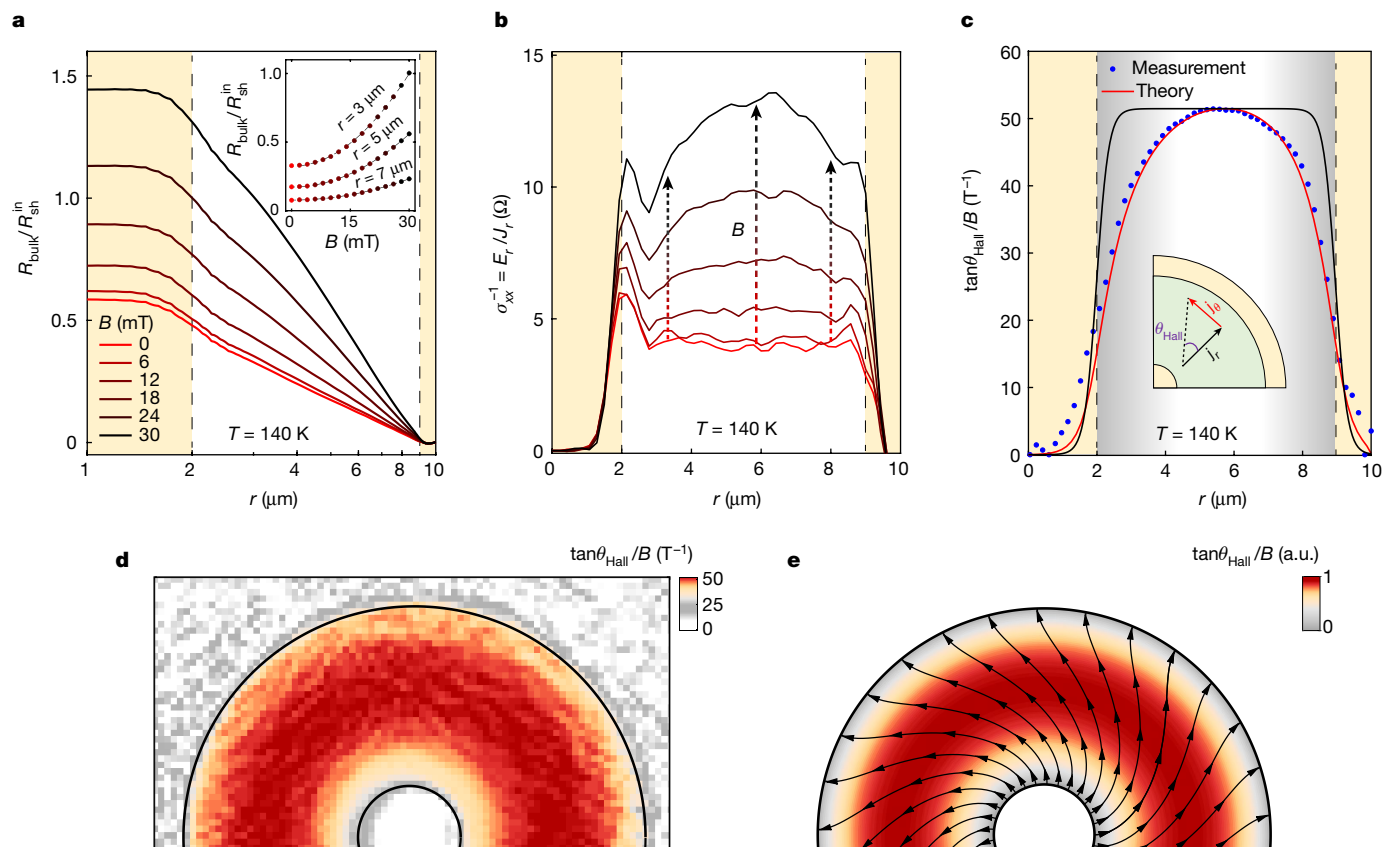


Fig. 4 | Imaging spiralling magneto-hydrodynamic electron flow and its Gurzhi boundary layer. **a**, $R_{\text{bulk}}(r)$, normalized by $R_{\text{sh}}^{\text{in}}$, measured at $T = 140$ K at various magnetic fields, B (see key). Inset: $R_{\text{bulk}}/R_{\text{sh}}^{\text{in}}$ at $r = 3, 5, 7 \mu\text{m}$ as a function of B . Dashed lines are parabolic fits. **b**, Inverse conductivity, $\sigma_{xx}^{-1} = E_r/j_r$ versus r at various B (same key as in **a**). $E_r = -d\phi/dr$ is the radial component of the electric field and $j_r = I/2\pi r$ is the current density. The rise of σ_{xx}^{-1} with B is larger at the centre of the channel than near the contacts (dashed arrows). **c**, Spatial dependence of the Hall angle, θ_{Hall} , obtained from fitting the quadratic-in- B term from **b** (see text). The figure plots $\tan(\theta_{\text{Hall}})/B$ (as θ_{Hall} is linear in B) versus r , plateauing at the centre of the channel and gradually dropping to zero toward the contacts. The drop occurs over a length scale significantly longer than our imaging resolution (black curve, obtained by convolving boxcar function with

the imaging PSF). The red curve is a fit to the magneto-hydrodynamic theory (see text). Inset: radial and angular current density, j_r and j_θ , and the Hall angle, θ_{Hall} . **d**, A full two-dimensional map of $\tan(\theta_{\text{Hall}})/B$ obtained by extracting at each spatial point (x, y) the quadratic-in- B dependence of σ_{xx}^{-1} (measured at $B = 0, 6, 12, 18, 24, 30$ mT). **e**, Theoretically calculated map of $\tan(\theta_{\text{Hall}})/B$ using the Navier–Stokes magneto-hydrodynamic equations and the parameters of the experiment in **c** and **d**, along with the calculated flow lines. At the centre of the channel, the flow lines are skewed from the radial direction by the standard Hall angle $\tan(\theta_{\text{Hall}}) = l_{\text{MR}}/R_c$ (R_c is the cyclotron radius). The boundary condition at the contacts dictates that $j_\theta = 0$ and thus $\theta_{\text{Hall}} = 0$. The climb of θ_{Hall} occurs over the Gurzhi length corresponding closely to the length scale that is seen in the experiment.

allowing for a direct mapping between the flow with ohmic scattering and the clean-limit flow: the measured profile $R_{\text{bulk}}(r)/R_{\text{sh}}^{\text{in}}$ with momentum-conserving and momentum-relaxing mean-free paths L_{ee} and L_{MR} is related to the clean-limit profile, $\tilde{R}_{\text{bulk}}(r)$, by a mere subtraction of an ohmic term (proof in Supplementary Section 13):

$$\tilde{R}_{\text{bulk}}(r)/R_{\text{sh}}^{\text{in}} = R_{\text{bulk}}(r)/R_{\text{sh}}^{\text{in}} - \frac{\hbar}{2e^2 k_{\text{F}} l_{\text{MR}}} \log(r_{\text{in}}/r) \quad (1)$$

The last term has only one free parameter, l_{MR} , which we determine directly from an independent magneto-hydrodynamic imaging experiment (see below). Equation (1) thus enables us to obtain $\tilde{R}_{\text{bulk}}(r)$ without adding any free parameters.

Figure 3b plots the obtained clean-limit hydrodynamic flow profiles, $\tilde{R}_{\text{bulk}}(r)$, at several temperatures. At low T , $\tilde{R}_{\text{bulk}}(r)$ follows the bulk Landauer–Sharvin dependence. With increasing T , however, this geometrical resistance gradually disappears. Remarkably, at $T = 140$ K and $T = 180$ K the profile is flat throughout most of the device’s bulk, apart from small regions (smaller than $1 \mu\text{m}$) near the contacts.

To interpret these measurements, we performed numerical Boltzmann calculations for a clean Corbino geometry with an electron–electron

mean-free path l_{ee} (Supplementary Section 14). Figure 3c shows the calculated $\tilde{R}_{\text{bulk}}(r)/R_{\text{sh}}^{\text{in}}$ for various l_{ee} values, smeared with the experimental PSF. For $l_{\text{ee}} = \infty$ the calculation recovers the Landauer–Sharvin dependence. With decreasing l_{ee} the Landauer–Sharvin resistance is gradually reduced. Once the electron–electron mean-free path becomes much shorter than the channel length, ($l_{\text{ee}} \ll r_{\text{out}} - r_{\text{in}}$), the resistive drop occurs only at a distance of around l_{ee} from the contacts, nicely matching the measurements at elevated temperatures. This is the hydrodynamic buildup distance, over which the electron–electron interactions rearrange the flow from ballistic to hydrodynamic. The calculations also reproduce the appearance of a resistive outer contact step with increasing T (Supplementary Section 15). Importantly, similar to the experimental result, we see that throughout most of the bulk of the disk the Landauer–Sharvin geometrical resistance is eliminated by the hydrodynamic flow.

Magneto-hydrodynamic flow: spiralling flow and imaging of the Gurzhi length

Finally, we explore magneto-hydrodynamic flow. Figure 4a shows the evolution of $R_{\text{bulk}}(r)$, measured at $T = 140$ K, with a perpendicular magnetic field, $B = 0$ – 30 mT. Even at such small fields, we see a notable $\propto B^2$

increase of the total resistance. This increase reflects the fact that in a Corbino geometry the ratio of the longitudinal electric field ($E_r = -\frac{d\phi}{dr}$) and current density ($j_r = \frac{I}{2\pi r}$) measure the inverse longitudinal conductivity, σ_{xx}^{-1} , rather than the longitudinal resistivity, ρ_{xx} (as in a Hall-bar geometry). Although these two quantities are similar at $B = 0$, at a finite field $\sigma_{xx}^{-1} = \rho_{xx}^{-1}(1 + \tan^2(\theta_{\text{Hall}}))$ obtains an additional Hall voltage component, originating from a linear-in- B angular current density, j_θ , leading to a Hall angle of $\tan(\theta_{\text{Hall}}) = j_\theta/j_r$ (Fig. 4c, inset). Figure 4b plots the measured $\sigma_{xx}^{-1} = E_r/j_r$, showing, that at $B = 0$, σ_{xx}^{-1} is independent of r across most of the disk's bulk, but it increases with B significantly more at the centre of the conducting channel than at its sides. By fitting the B dependence at each r we obtain the position dependence of $\tan(\theta_{\text{Hall}})$ (Fig. 4c), exhibiting a maximum at the centre of the channel and a gradual drop towards the contacts. The length scale of this drop is much longer than our resolution limit (black line, Fig. 4c) and than the scale of l_{ee} (seen in Fig. 3b). Measuring $\tan(\theta_{\text{Hall}})$ in the full two-dimensional plane (Fig. 4d) shows a similar behaviour: the Hall angle is largest at the centre of the conducting channel, and gradually drops towards the contacts. Thus, at finite fields, we observe a new length scale that describes the spatial change of θ_{Hall} .

Such an emergent length scale was proposed by recent theories of magneto-hydrodynamic flow in a Corbino geometry^{19,31}, whose flow lines are reproduced in Fig. 4e. At the centre of the conducting channel, these lines are slanted with respect to the radial by the standard Hall angle, $\tan(\theta_{\text{Hall}}) = \frac{l_{\text{MR}}}{R_c}$ (R_c is the cyclotron radius). However, near the contacts θ_{Hall} goes to zero, because the electrons are injected from the contacts isotropically, namely $j_\theta = 0$. The theory gives:

$$\tan(\theta_{\text{Hall}}) = \frac{l_{\text{MR}}}{R_c} + C_1 I_1\left(\frac{r}{l_G}\right) + C_2 r K_1\left(\frac{r}{l_G}\right), \quad (2)$$

where I_1, K_1 are the modified Bessel functions, C_1, C_2 are constants chosen such that $\tan(\theta_{\text{Hall}}) = 0$ at $r = r_{\text{in}}, r_{\text{out}}$, and $l_G = \sqrt{l_{\text{MR}} l_{\text{ee}}/4}$ is the Gurzhi length. The red curve in Fig. 4c plots the theory profile for $l_{\text{MR}} = 4.35 \mu\text{m}$ and $l_{\text{ee}} = 1.3 \mu\text{m}$, which agrees best with the experiment. This l_{MR} is dominated by electron-phonon coupling and agrees well with earlier measurements in clean samples^{12,14,35,37}. Moreover, the l_{ee} obtained from the $B = 0$ experiment (Fig. 3) and from the magneto-hydrodynamic experiment (Fig. 4) closely agree, although they have completely different manifestations in these two flow regimes: in the former, l_{ee} gives the hydrodynamic buildup length, whereas in the latter, l_{ee} enters only through its geometrical average with l_{MR} to give the spatial scale of the θ_{Hall} gradient. Notably, this key emergent length of electron hydrodynamics theory, the Gurzhi length, is observed here directly.

Online content

Any methods, additional references, Nature Research reporting summaries, source data, extended data, supplementary information, acknowledgements, peer review information; details of author contributions and competing interests; and statements of data and code availability are available at <https://doi.org/10.1038/s41586-022-05002-7>.

- Landauer, R. Spatial variation of currents and fields due to localized scatterers in metallic conduction. *IBM J. Res. Dev.* **1**, 223–231 (1957).
- Sharvin, Y. V. A. Possible method for studying Fermi surfaces. *Sov. Phys. JETP* **21**, 655 (1965).
- de Jong, M. J. M. & Molenkamp, L. W. Hydrodynamic electron flow in high-mobility wires. *Phys. Rev. B* **51**, 389–402 (1995).
- Bandurin, D. A. et al. Negative local resistance caused by viscous electron backflow in graphene. *Science* **351**, 1055–1058 (2016).

- Crossno, J. et al. Observation of the Dirac fluid and the breakdown of the Wiedemann-Franz law in graphene. *Science* **351**, 1058–1061 (2016).
- Moll, P. J. W., Kushwaha, P., Nandi, N., Schmidt, B. & Mackenzie, A. P. Evidence for hydrodynamic electron flow in PdCoO₂. *Science* **351**, 1061–1064 (2016).
- Krishna Kumar, R. et al. Superballistic flow of viscous electron fluid through graphene constrictions. *Nat. Phys.* **13**, 1182–1185 (2017).
- Gooth, J. et al. Thermal and electrical signatures of a hydrodynamic electron fluid in tungsten diphosphide. *Nat. Commun.* **9**, 4093 (2018).
- Braem, B. A. et al. Scanning gate microscopy in a viscous electron fluid. *Phys. Rev. B* **98**, 241304 (2018).
- Berdugin, A. I. et al. Measuring Hall viscosity of graphene's electron fluid. *Science* **364**, 162–165 (2019).
- Tan, C. et al. Realization of a universal hydrodynamic semiconductor in ultra-clean dual-gated bilayer graphene. *Sci. Adv.* **8**, eabi8481 (2022).
- Sulpizio, J. A. et al. Visualizing Poiseuille flow of hydrodynamic electrons. *Nature* **576**, 75–79 (2019).
- Ku, M. J. H. et al. Imaging viscous flow of the Dirac fluid in graphene. *Nature* **583**, 537–541 (2020).
- Jenkins, A. et al. Imaging the breakdown of ohmic transport in graphene. Preprint at <https://arxiv.org/abs/2002.05065> (2020).
- Keser, A. C. et al. Geometric control of universal hydrodynamic flow in a two-dimensional electron fluid. *Phys. Rev. X* **11**, 031030 (2021).
- Gupta, A. et al. Hydrodynamic and ballistic transport over large length scales in GaAs/AlGaAs. *Phys. Rev. Lett.* **126**, 076803 (2021).
- Krebs, Z. J. et al. Imaging the breaking of electrostatic dams in graphene for ballistic and viscous fluids. Preprint at <https://arxiv.org/abs/2106.07212> (2021).
- Vool, U. et al. Imaging phonon-mediated hydrodynamic flow in WTe₂. *Nat. Phys.* <https://doi.org/10.1038/s41567-021-01341-w> (2021).
- Shavit, M., Shytov, A. & Falkovich, G. Freely flowing currents and electric field expulsion in viscous electronics. *Phys. Rev. Lett.* **123**, 026801 (2019).
- Stern, A. et al. Spread and erase – how electron hydrodynamics can eliminate the Landauer-Sharvin resistance. Preprint at <https://arxiv.org/abs/2110.15369?context=cond-mat.str-el> (2021).
- Gurzhi, R. N. Minimum of resistance in impurity free conductors. *Sov. Phys. JETP* **17**, 521 (1963).
- Nagaev, K. E. & Ayyvazyan, O. S. Effects of electron-electron scattering in wide ballistic microcontacts. *Phys. Rev. Lett.* **101**, 1–4 (2008).
- Nagaev, K. E. & Kostyuchenko, T. V. Electron-electron scattering and magnetoresistance of ballistic microcontacts. *Phys. Rev. B* **81**, 1–9 (2010).
- Andreev, A. V., Kivelson, S. A. & Spivak, B. Hydrodynamic description of transport in strongly correlated electron systems. *Phys. Rev. Lett.* **106**, 256804 (2011).
- Torre, I., Tomadin, A., Geim, A. K. & Polini, M. Nonlocal transport and the hydrodynamic shear viscosity in graphene. *Phys. Rev. B* **92**, 165433 (2015).
- Levitov, L. & Falkovich, G. Electron viscosity, current vortices and negative nonlocal resistance in graphene. *Nat. Phys.* **12**, 672–676 (2016).
- Scaffidi, T., Nandi, N., Schmidt, B., Mackenzie, A. P. & Moore, J. E. Hydrodynamic electron flow and Hall viscosity. *Phys. Rev. Lett.* **118**, 226601 (2017).
- Guo, H., Ilse, E., Falkovich, G. & Levitov, L. S. Higher-than-ballistic conduction of viscous electron flows. *Proc. Natl Acad. Sci. USA* **114**, 3068–3073 (2017).
- Narozhny, B. N., Gornyi, I. V., Mirlin, A. D. & Schmalian, J. Hydrodynamic approach to electronic transport in graphene. *Ann. Phys.* **529**, 1700043 (2017).
- Holder, T. et al. Ballistic and hydrodynamic magnetotransport in narrow channels. *Phys. Rev. B* **10**, 245305 (2019).
- Levchenko, A. & Schmalian, J. Transport properties of strongly coupled electron-phonon liquids. *Ann. Phys.* **419**, 168218 (2020).
- Hong, Q., Davydova, M., Ledwith, P. J. & Levitov, L. Superscreening by a retroreflected hole backflow in tomographic electron fluids. Preprint at <https://arxiv.org/abs/2012.03840> (2020).
- Honig, M. et al. Local electrostatic imaging of striped domain order in LaAlO₃/SrTiO₃. *Nat. Mater.* **12**, 1112–1118 (2013).
- Ella, L. et al. Simultaneous voltage and current density imaging of flowing electrons in two dimensions. *Nat. Nanotechnol.* **14**, 480–487 (2019).
- Wang, L. et al. One-dimensional electrical contact to a two-dimensional material. *Science* **342**, 614–617 (2013).
- Ben Shalom, M. et al. Quantum oscillations of the critical current and high-field superconducting proximity in ballistic graphene. *Nat. Phys.* **12**, 318–322 (2016).
- Efetov, D. K. & Kim, P. Controlling electron-phonon interactions in graphene at ultrahigh carrier densities. *Phys. Rev. Lett.* **105**, 256805 (2010).

Publisher's note Springer Nature remains neutral with regard to jurisdictional claims in published maps and institutional affiliations.

Springer Nature or its licensor holds exclusive rights to this article under a publishing agreement with the author(s) or other rightsholder(s); author self-archiving of the accepted manuscript version of this article is solely governed by the terms of such publishing agreement and applicable law.

© The Author(s), under exclusive licence to Springer Nature Limited 2022

Methods

Device fabrication

Scanning SET devices were fabricated using a nanoscale assembly technique³⁸. The graphene/hBN devices were fabricated using electron-beam lithography and standard etching and nanofabrication procedures³⁵ to define the channels and evaporation of Cr/Au (Supplementary Section 4) to deposit contact electrodes.

Measurements

The measurements were performed on multiple graphene devices in home-made, variable temperature, Attocube-based scanning probe microscopes. The microscopes operate in vacuum inside a liquid-helium dewar with superconducting magnets, and are mechanically stabilized using Newport laminar flow isolators. A local resistive SMD heater was used to heat the samples under study from $T = 7.5$ K to $T = 180$ K, and a DT-670-BR bare chip diode thermometer mounted proximally to the samples and on the same printed circuit boards was used for precise temperature control. The voltage imaging technique used is presented in ref.³⁴. Voltages and currents (for both the SET and sample under study) were sourced using a home-made data acquisition card array and measured using a home-made, software-based audio-frequency lock-in amplifier consisting of 1 μ V accurate d.c. plus a.c. sources and a Femto DPLCA-200 current amplifier and NI-9239 ADC. The local gate voltage of the SET was dynamically adjusted by custom feedback electronics using a least-squares regression algorithm to prevent disruption of the working point of the SET during scanning and to ensure reliable measurements.

The voltage excitations applied to the graphene channels were as follows: 1 mV at $T = 6$ K, and 8 mV at $T = 180$ K. The magnetic fields applied ranged between ± 30 mT.

Data availability

Source data are provided with this paper. Additional data that support the plots and other analysis in this work are available from the corresponding author upon request.

38. Waissman, J. et al. Realization of pristine and locally tunable one-dimensional electron systems in carbon nanotubes. *Nat. Nanotechnol.* **8**, 569–574 (2013).

Acknowledgements We thank L. Ella, G. Falkovich, L. Levitov, M. Polini, M. Shavit, A. Rozen, A. V. Shytov and U. Zondiner for useful discussions. Work was supported by the Leona M. and Harry B. Helmsley Charitable Trust grant, ISF grant (no. 1182/21), Minerva grant (no. 713237), Hydrotronics (no. 873028) and the ERC-Cog (See-1D-Qmatter, no. 647413). T.S. acknowledges the support of the Natural Sciences and Engineering Research Council of Canada (NSERC), in particular the Discovery Grant (no. RGPIN-2020-05842), the Accelerator Supplement (no. RGPAS-2020-00060) and the Discovery Launch Supplement (no. DGEER-2020-00222). During the preparation of this manuscript, we became aware of a partially related STM work¹⁷, which images voltage drops in flows across a constriction.

Author contributions C.K., J.B., J.A.S., A.K.G. and S.I. designed the experiment. C.K., J.B. and J.A.S. performed the experiments. J.B. and D.P. fabricated the devices. C.K., J.B., J.A.S. and S.I. analysed the data. T.S., A.S. and S.I. wrote the theoretical model. K.W. and T.T. supplied the hBN crystals. C.K., J.B., A.S. and S.I. wrote the manuscript with input from other authors.

Competing interests The authors declare no competing interests.

Additional information

Supplementary information The online version contains supplementary material available at <https://doi.org/10.1038/s41586-022-05002-7>.

Correspondence and requests for materials should be addressed to S. Ilani.

Peer review information *Nature* thanks Yonglong Xie and the other, anonymous, reviewer(s) for their contribution to the peer review of this work.

Reprints and permissions information is available at <http://www.nature.com/reprints>.